Microbial feedbacks optimize ocean iron availability

Jonathan Maitland Lauderdale[a,1], Rogier Braakman[a,b], Gaël Forget[a], Stephanie Dutkiewicz[a,c], and Michael J. Follows[a,b]

[a]Department of Earth, Atmospheric and Planetary Sciences, Massachusetts Institute of Technology, Cambridge, MA 02139; [b]Department of Civil and Environmental Engineering, Massachusetts Institute of Technology, Cambridge, MA 02139; and [c]Center for Global Change Science, Massachusetts Institute of Technology, Cambridge, MA 02139

Edited by Inez Fung, University of California, Berkeley, CA, and approved January 22, 2020 (received for review October 4, 2019)

Iron is the limiting factor for biological production over a large fraction of the surface ocean because free iron is rapidly scavenged or precipitated under aerobic conditions. Standing stocks of dissolved iron are maintained by association with organic molecules (ligands) produced by biological processes. We hypothesize a positive feedback between iron cycling, microbial activity, and ligand abundance: External iron input fuels microbial production, creating organic ligands that support more iron in seawater, leading to further macronutrient consumption until other microbial requirements such as macronutrients or light become limiting, and additional iron no longer increases productivity. This feedback emerges in numerical simulations of the coupled marine cycles of macronutrients and iron that resolve the dynamic microbial production and loss of iron-chelating ligands. The model solutions resemble modern nutrient distributions only over a finite range of prescribed ligand source/sink ratios where the model ocean is driven to global-scale colimitation by micronutrients and macronutrients and global production is maximized. We hypothesize that a global-scale selection for microbial ligand cycling may have occurred to maintain "just enough" iron in the ocean.

dissolved iron | organic ligands | ocean productivity | macronutrients | colimitation

Iron, nitrogen, carbon, and other elements in the surface ocean are consumed by microbes, leading to a flux of sinking and subducted organic matter that is respired in deeper waters, ultimately releasing those nutrients back into dissolved (inorganic) form. Ocean circulation returns resource-rich deep waters back to the surface layer, maintaining global ocean productivity and sustaining a biologically mediated reservoir of inorganic carbon at depth, drawing down atmospheric CO_2.

Oceanic primary production may be constrained by one of several key resources. Nutrient addition experiments have shown that most of the surface ocean is locally limited by the availability of either fixed nitrogen or iron (1–6). On a global scale, the strength of biological ocean carbon storage can be determined by the efficiency of macronutrient use, the fraction (0 to 1) of dissolved inorganic nutrients in the abyss resulting from remineralization of sinking and subducted organic matter (7, 8). Low efficiency indicates that macronutrients in the deep ocean arrive there by physical transport, while high efficiency indicates that biological export dominates. Evaluated from observations, modern macronutrient use efficiency is ∼0.36 (9), confirming that the biosphere is prevented from fully consuming macronutrients at the surface. Indeed, iron availability is the primary limiting factor for production over about half of the surface ocean (10–12), and therefore the global ocean might be broadly considered colimited by iron and macronutrients.

Although plentiful on Earth, ferric iron, Fe(III), has trace concentrations in the ocean because of its low solubility in oxygen-rich waters [0.01 nM (13)]. Due to rapid precipitation or scavenging, iron has a short residence time compared to macronutrients, around 100 y (14, 15), so older upwelling waters are typically depleted in iron but macronutrient-rich, leading to iron limitation in the southern, equatorial, and sub-Arctic Pacific "high-nutrient, low-chlorophyll" oceans.

The conclusion that oceanic production is colimited by macronutrients and iron is also supported by modeling studies exploring responses to changing iron supply (e.g., refs. 10 and 16–21). Stimulated by interest in iron fertilization to mitigate anthropogenic CO_2 emissions or as a driver of past climate, models have generally found net global productivity responds only moderately or weakly to changing iron inputs. High latitudes appear to be close to local limitation by iron and light, while, globally, relieving iron limitation in one region leads to compensating macronutrient limitation in adjacent areas (22). Thus, while observations often suggest local iron limitation (1–3), the complex dynamics of global simulations highlight an interplay between different resources that shape the patterns of productivity in the oceans.

Why is the global ocean poised at a state of colimitation between iron and macronutrients? We argue that it is because marine organisms can modify the residence time of iron in the oceans. Most oceanic dissolved iron (<0.2-μm filter) is associated with organic chelating ligands (23–31), organic molecules that bind to iron and act as a refuge from loss by scavenging and precipitation. The specific nature of ligands is difficult to characterize (32), with bulk abundance and conditional stability coefficients typically inferred electrochemically (e.g., refs. 23–26 and 28–38). These studies reveal multiple classes of ligand with different binding affinities, concentrations, and distributions. This spectrum of organic chelators includes, but is not limited to, siderophores, which are strong-binding molecules secreted by microbes to competitively capture iron (39–41), and weaker-binding molecules that have an affinity for iron, like

Significance

Marine microbe growth is limited by iron over about half of the global ocean surface. Dissolved iron is quickly lost from the ocean, but its availability to marine microbes may be enhanced by binding with organic molecules which, in turn, are produced by microbes. We hypothesize this forms a reinforcing cycle between biological activity and iron cycling that locally matches the availability of iron and other nutrients, leading to global-scale resource colimitation between macronutrients and micronutrients, and maximizing biological productivity. Idealized models support this hypothesis, depending on the specific relationships between microbial sources and sinks of organic molecules. An evolutionary selection may have occurred which optimizes these characteristics, resulting in "just enough" iron in the ocean.

Author contributions: J.M.L., R.B., and M.J.F. designed research; J.M.L. and M.J.F. performed research; J.M.L., G.F., and S.D. analyzed data; and J.M.L., R.B., G.F., S.D., and M.J.F. wrote the paper.

The authors declare no competing interest.

This article is a PNAS Direct Submission.

Data deposition: Model code, output, and processing routines can be accessed via GitHub (http://bit.ly/lauderdale-ligand-iron-microbe-feedback).

[1]To whom correspondence may be addressed. Email: jml1@mit.edu.

First published February 18, 2020.

exuded polysaccharides, porphyrins, degraded protein remnants, and humic substances (23–27, 38, 42–46). Ligand production is likely heterogenous in space and time: Siderophore synthesis occurs under iron stress (40), but elevated ligand levels have been documented following experimental iron addition (24, 44, 47, 48), suggesting other ligand production pathways.

The Ligand–Iron–Microbe Feedback

Given the organic origin of iron-binding chelators, we hypothesize that a positive feedback between microbial activity, ligand abundance, and iron availability could emerge (Fig. 1). Iron is supplied by dust deposition, sediment mobilization, and hydrothermal activity. In a hypothetical watermass where ligand abundance is initially very low, Fe(III) is largely insoluble, but a small population of microbes subsist. Their turnover produces ligands such as siderophores, excreted organic carbon, or chelating detritus. Greater ligand abundance retains more iron in seawater, incrementally relieving iron limitation, promoting further biological production, and so on. Eventually, other requirements, such as macronutrients, become limiting (Fig. 1), and additional iron no longer increases productivity. At appropriate time and space scales, the global ligand pool is regulated, supporting "just enough" iron to match availability of other resources redistributed by ocean circulation, maximizing overall nutrient consumption and global productivity.

In the following, we show that such a feedback does emerge in an idealized three-box ocean biogeochemistry model that resolves a dynamic pool of iron-binding ligands.

Model Framework

The model (Fig. 2) represents an ocean with an overturning circulation linking a low iron input, upwelling regime, analogous to the "high-nutrient, low-chlorophyll" regions of the ocean, to a high iron input, deep water formation regime. In this idealized system, we consider two basins, which we will refer to as the "Southern Ocean" and "Atlantic Ocean," respectively, but the overall concepts could equally apply to other regions. Further details are given in *Materials and Methods*.

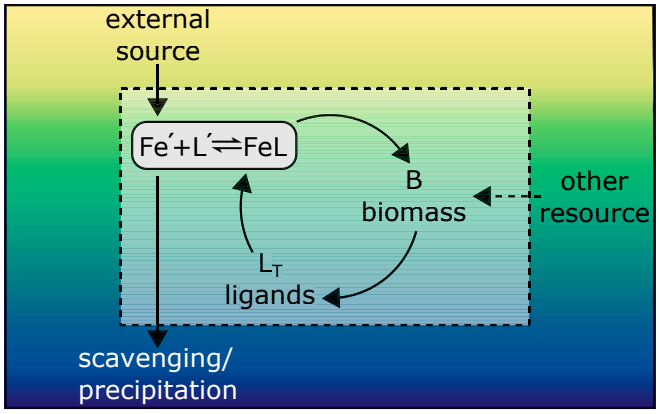

Fig. 1. Schematic of the "ligand–iron–microbe" feedback. Free iron (*Fe′*) is added to the ocean from external sources like dust and sedimentary mobilization, and lost due to scavenging, precipitation, and burial. Iron retention is increased by complexation with organic ligands (L_T; $Fe_T = Fe' + FeL$ and $L_T = L' + FeL$). Microbial production of biomass (*B*) is dependent on iron, and is a source of ligands, for example, by siderophore production, excretion of organic carbon, and release of cell detritus during remineralization. The production of ligands retains a greater concentration of iron, fueling more microbial production, and so on, until the other resources that microbial production requires, such as macronutrients, become limiting. Thus the "ligand–iron–microbe" feedback maintains "just enough" iron in the ocean to match the availability of other resources, resulting in colimitation.

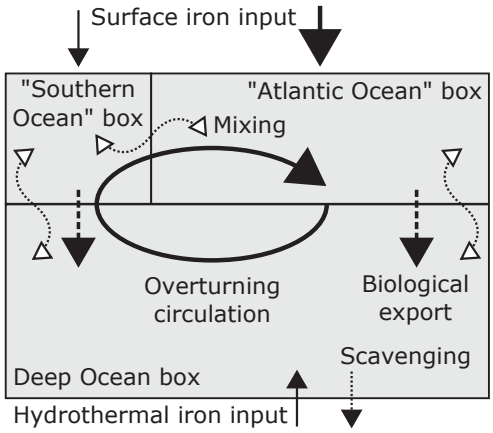

Fig. 2. Schematic of the idealized three-box ocean biogeochemistry model. See text and *Materials and Methods* for further details.

Microbial net production (B, moles N per cubic meter per second) in the upper ocean consumes macronutrients (N, dissolved inorganic nitrogen, moles per cubic meter), and total dissolved iron (Fe_T, moles per cubic meter) using Michaelis–Menten kinetics (Eq. **1**). The maximum rate, α, is limited by N, Fe_T, or light (I, watts per square meter) levels (with coefficients k_N, k_{Fe}, and k_I).

$$B = \alpha \frac{I}{k_I + I} min\left(\frac{N}{k_N + N}, \frac{Fe_T}{k_{Fe} + Fe_T}\right). \quad [1]$$

This fixed organic material has Redfield stoichiometry ($R_{\mathrm{C:N:P:Fe}} = 106{:}16{:}1{:}1\times10^{-3}$). Coupled macronutrient and iron cycles (Eqs. **2** and **3**) are solved following ref. 49. Defining the substantial derivative including ocean transport (ψ) and mixing (κ) of tracer, A, as $DA/Dt = \partial A/\partial t + \nabla\cdot(\psi A) - \nabla\cdot(\kappa\nabla A)$ in moles A per cubic meter per second, the governing equations in each model box (see text below for definitions) are

$$\frac{DN}{Dt} = -\mathcal{H}B \quad [2]$$

$$\frac{DFe_T}{Dt} = s_{Fe} - R_{\mathrm{Fe:N}}\mathcal{H}B - k_s Fe' \quad [3]$$

$$\frac{DL_T}{Dt} = \gamma R_{\mathrm{C:N}} B - \lambda L_T. \quad [4]$$

N and Fe_T are taken up by biological activity at the surface, exported to the deep box, and completely remineralized ($\mathcal{H}$ is a step function: +1 at the surface and −1 at depth). The global N inventory is assumed constant in this idealized model.

Iron is supplied to the surface (s_{Fe}, moles Fe per cubic meter per second), representing aeolian (50) or shelf sediment (51) sources, with 100 times less entering the "Southern Ocean" than "Atlantic Ocean" boxes (50, 52). A hydrothermal iron source is also added to the deep box (53).

For illustrative purposes, we consider a single, representative pool of total ligand (L_T, moles per cubic meter; Eq. **4**) with a conditional stability coefficient that determines the partitioning between free and complexed iron (49). Free iron (Fe', moles per cubic meter) is scavenged and precipitated when in excess of its low solubility with rate constant k_s (per second).

Ligands are produced as a fraction (γ, moles L per moles C) of organic matter turnover in both surface and deep ocean associated with net production in the surface layer, portraying exudate release (27) and siderophore production (54), and deep ocean remineralization of sinking particulate organic matter (46), such

as release of porphyrins and degraded protein chelators. Ligand loss is a first-order process with rate λ (per second), associated with microbial degradation. The prescribed rate of loss is modified to be 100 times longer in the deep box than in the surface boxes (55) to account for the gradient introduced by enhanced depletion through photochemical degradation (24, 56) and microbial uptake (57) in the upper ocean, slower losses at depth due to an order of magnitude decrease in bacterial abundance (58), and slower metabolism resulting from cooler temperatures.

In reality, ligands are diverse and only partially characterized (e.g., refs. 32 and 34), so we have little direct constraint on their source and sink rates (i.e., γ and λ values). At steady state, when transport terms are constant ($DL_T/Dt \approx 0$), Eq. **4** implies a relationship between the representative ligand source/sink rates (γ and λ) and measurable bulk characteristics of the whole ocean,

$$\frac{\gamma}{\lambda} \approx \frac{L_T}{R_{\mathrm{C:N}} B}. \qquad [5]$$

We can approximate a likely range of γ/λ from an observational perspective by substituting $R_{\mathrm{C:N}}B$ in Eq. **5** with an order of magnitude estimate of global oceanic net production [10 GtC· y^{-1} to 100 GtC· y^{-1} (59)], and observed ligand concentrations (L_T) between ~0.6 μmol·m^{-3} and 6 μmol·m^{-3} (e.g., refs. 29–31, 52, and 60), in the open ocean. First, converting net production into concentration units by distributing the integrated estimate (59) over either mixed layer volume or full ocean volume (61) gives $\gamma/\lambda \approx L_T/R_{C:N}B \approx 1.6\times10^{2}$–$3\times10^{5}$ s. An equivalent range is found using the same mixed layer volume over which organic carbon production occurs and accounting for the gradient in λ, assuming deep ocean values are 100 times smaller than prescribed surface values.

The ligand to organic carbon ratio (γ) has been estimated between 1×10^{-5} mol L·(mol C)$^{-1}$ and 10×10^{-5} mol L·(mol C)$^{-1}$ (46, 62–64). Combining these γ values with our approximate range of $L_T/R_{C:N}B$ leads to ligand decay rates (λ) of 3.2×10^{-11} s^{-1} to 6.1×10^{-7} s^{-1}, or ligand turnover times ($1/\lambda$) between 20 d and 960 y. These bulk values fall within a range of degradation timescale estimates for partially labile and semirefractory dissolved organic carbon [1 y to 1,000 y (64)], and have an upper bound (e.g., ref. 31) consistent with estimates of the residence time of ligands in deep waters of the Atlantic [779 y to 1,039 y (30)].

Illustration of the Ligand–Iron–Microbe Feedback

The emergent "ligand–iron–microbe" feedback can be cleanly illustrated with a single model equilibration time series (Fig. 3). The model is initialized with globally uniform macronutrient concentrations (33 mmol N·m^{-3}) and no dissolved iron or ligands, then integrated for 10,000 y. Ligand characteristics are set such that $\gamma/\lambda = 4{,}500$ s. Initially, the model is iron-limited globally, with elevated macronutrients in both "Atlantic Ocean" and "Southern Ocean" surface boxes (Fig. 3*A*). Relatively high iron delivery to the "Atlantic Ocean" box leads to an initial rise in productivity (Fig. 3*D*) and depletion of surface macronutrients (Fig. 3*A*). This drives ligand production (Fig. 3*B*), allowing accumulation of a standing stock of deep ocean iron (Fig. 3*C*). In the following centuries, macronutrients stay depleted with elevated productivity, and "North Atlantic" ligand levels converge toward steady state due to transport and loss processes.

In contrast, lower iron input to the "Southern Ocean" box cannot support rapid macronutrient drawdown. On longer timescales, as ligand levels increase throughout the ocean, upwelled chelated iron drives a gradual incomplete reduction of surface macronutrients.

Steady state is reached after 1,000 y. The "Southern Ocean" box is iron-limited (Fig. 3*C*), with incomplete macronutrient use

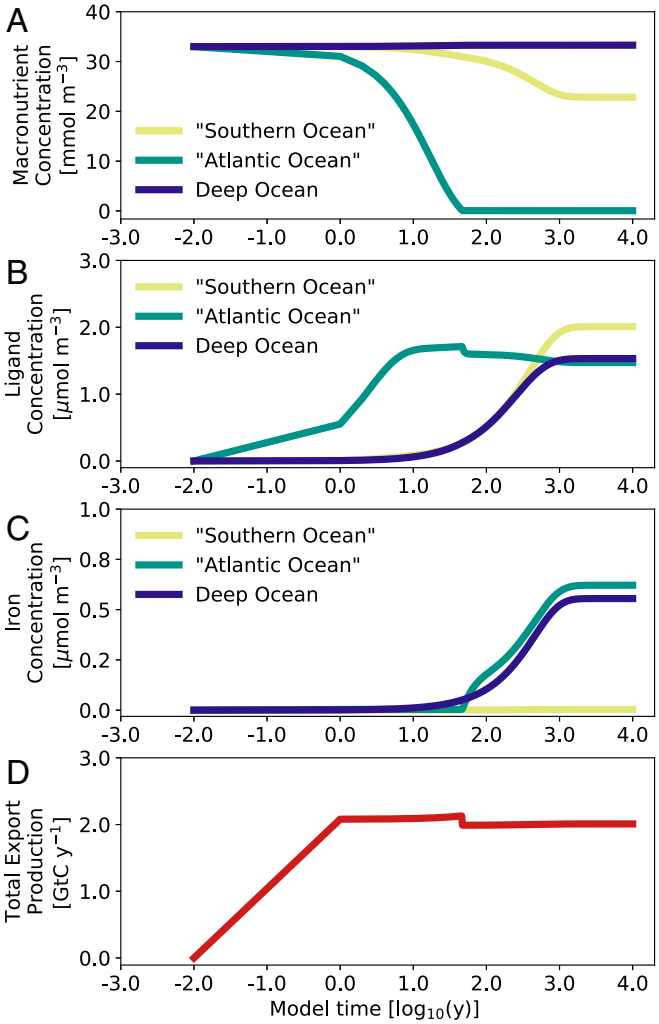

Fig. 3. Illustration of the "ligand–iron–microbe" feedback: 10,000-y time series (note the log-scale axis) of (*A*) macronutrient, (*B*) dissolved iron, and (*C*) ligand concentrations in the "Southern Ocean" box (yellow), "Atlantic Ocean" box (green), and Deep Ocean box (blue), and (*D*) globally integrated export production. Steady state is reached after 1,000 y. The model is initialized with uniform 33 mmol N·m^{-3} of macronutrients and no iron and ligands, with $\gamma/\lambda \approx$ 4,500 s ($\gamma = 5\times10^{-5}$ mol L·(mol C)$^{-1}$ and $1/\lambda \approx 3$ y from the observationally constrained range).

(Fig. 3*A*) fueled by iron supply from the deep ocean, while the "Atlantic Ocean" box is macronutrient-limited, with sufficient iron to fully consume macronutrients primarily delivered by the overturning circulation.

Therefore, using ligand source and sink rates guided by present-day observations (i.e., constraining γ/λ), we demonstrated an emergent positive feedback that promotes global-scale iron and macronutrient colimitation with uniform ligand distribution (~2 μmol·m^{-3}) and slightly elevated ligand abundance in the upwelling box, reminiscent of the modern ocean (31, 60, 64).

How robust is this result? The next section presents a suite of simulations over a wide range of γ/λ and initial conditions.

Robustness of the Feedback: A Large Model Ensemble

A suite of 10,000 simulations of the three-box ocean biogeochemistry model was integrated for 10,000 y each, with independently assigned values (Fig. 4*A*) of γ between 1×10^{-7} mol L·(mol C)$^{-1}$ and 1×10^{-1} mol L·(mol C)$^{-1}$ and $1/\lambda$ between 0.1 y and 1,000 y. This range of γ/λ extends far beyond

that inferred for the modern ocean. Integrations start with random initial concentrations of iron, ligand, and macronutrients (but the same total macronutrient inventory).

Results are summarized in Fig. 4*B*, which shows the envelopes of globally averaged, steady-state surface nutrient concentrations as a function of γ/λ, and Fig. 4*C*, which shows envelopes of export production rate in each box, as well as the global total. It is notable that the concentrations and rates of microbial production converge to a tight curve as a function of γ/λ while representing numerous combinations of individual γ and λ values, as well as a range of random arbitrary initial conditions. In other words, the outcomes are robust and predictable for any given γ/λ, and independent of initial conditions: The feedback restores the degree of biological limitation between macronutrients and iron for the specific value of γ/λ, in the same way as in the time series shown in Fig. 3.

The 10,000 simulations fall into three groups that express fundamentally different nutrient regimes (Fig. 4 *B* and *C*):

1) The first is an iron-limited regime with relatively low γ/λ that cannot accumulate a sufficient ligand pool due to low ligand production or high rates of ligand decay. The standing stock of iron is very low, and any iron input (particularly in the "Atlantic Ocean" box) is rapidly consumed or lost to scavenging, leaving surface macronutrients incompletely used. Resulting export production, largely in the "Atlantic Ocean" box, is low.
2) The second is an iron-replete regime, with relatively high γ/λ and a large ligand pool due to rapid ligand production or slow decay rates. This supports maximum iron abundance (set by total external iron input accumulated over 10,000 y) relieving limitation even in the "Southern Ocean" box, which receives little external iron input. Surface macronutrients are low and export production is high, predominantly in the "Southern Ocean" box where nutrients are upwelled by the overturning circulation.
3) The third is an iron and macronutrient colimited regime in which the "ligand–iron–microbe" feedback restores the system to global-scale colimitation, with both macronutrient- and iron-limited regions. Ligand abundance supports sufficient iron levels to obtain near-maximum global export production rates mediated by macronutrient, iron, and ligand redistribution via ocean circulation, as in Fig. 3.

In short, simulations fall into three robust regimes, governed by the characteristic ratio of ligand source and sink rates. Global colimitation, with regional limiting resource variation, is subject to a reinforcing feedback if ligand characteristics are in the appropriate regime, but it is not inevitable.

Where does the modern ocean fit into this continuum? We scored ensemble members by quantitative comparison to oceanic observations (S: possible range 0 to 1; Fig. 5*A* and *Materials and Methods*) taking the median of scores for simulations with the same γ/λ (Fig. 5*B*). Scores were compared to a benchmark ($S = 0.69$) evaluated from a model simulation where ligand concentration was held fixed at a uniform, global value of 1 $\mu mol \cdot m^{-3}$ (as employed in global biogeochemistry models; e.g., ref. 65). Dynamic ligand simulations with model–data comparison scores greater than the benchmark value are outperforming the standard parameterization. The best scores are obtained in a band of intermediate γ/λ with moderate levels of macronutrients, iron, and ligands. The optimum $\log_{10}(\gamma/\lambda)$ value is 3.643 (γ/λ = 4,398 s) with a score of 0.81 (Fig. 5*B*).

Macronutrient use efficiency was diagnosed as the fraction of macronutrients transported from the surface to the deep by biological activity (7–9). Efficiency of macronutrient use is positively correlated with γ/λ (Fig. 5 *A* and *C*), and reflects the pattern of export production in the low-iron, upwelling "Southern Ocean" box (Fig. 4*C*; e.g., refs. 66 and 67). Model solutions exceeding the benchmark score have efficiencies of 0.22 to 0.40, with an optimum of 0.29 at the model–data best fit (Fig. 5*C*).

Discussion

Iron availability in the modern, oxygen-rich, ocean is intimately tied to the cycling of organic chelating ligands, and so could form a reinforcing cycle: Production of ligands enhances the availability of iron, in turn increasing biological activity, leading to further production of ligands. Logically, this feedback should be halted when another resource becomes limiting (Fig. 1). In other words, the feedback drives the system toward global macronutrient and micronutrient colimitation and maximum net productivity, mediated by macronutrient, iron, and ligand redistribution via ocean circulation (Fig. 3).

We explored this emergent "ligand–iron–microbe" feedback in an idealized ocean biogeochemistry model with a dynamic

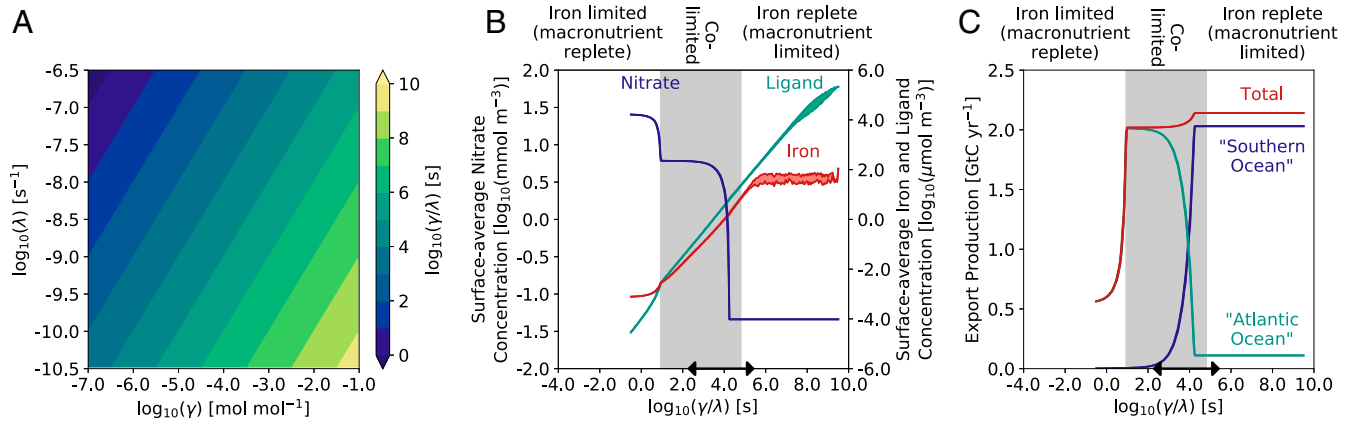

Fig. 4. Ensemble of 10,000 box model simulations. (*A*) Range of prescribed γ and λ values, (*B*) envelope of resulting surface nitrate (blue), iron (red), and ligand (green) concentrations, and (*C*) envelope of export production rates for the "Southern Ocean" box (blue), "Atlantic Ocean" box (green), and global total (red). Envelopes are calculated from median values of simulations with equal γ/λ ratios, that is, averaged within colored contours in Fig. 4*A* ± the median absolute deviation (note the log scales). The range of γ/λ informed by oceanic observations is indicated by arrows on the *x* axis. Guided by these data, the experiments can be partitioned into three regimes: 1) iron-replete (macronutrient limited) simulations, 2) iron-limited (macronutrient replete) simulations, and 3) iron and macronutrient colimited simulations (region shaded gray)—see text for details.

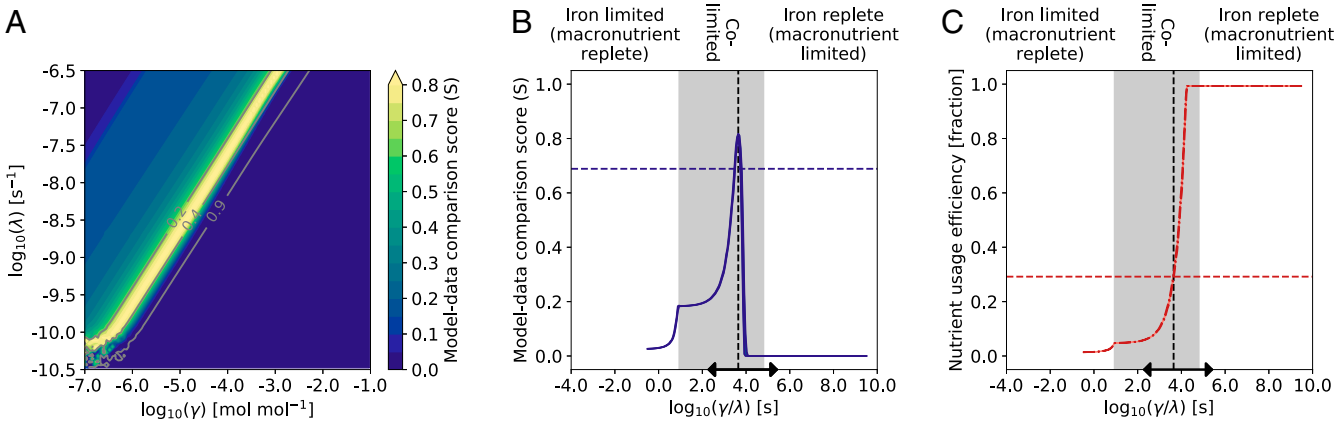

Fig. 5. Ensemble of 10,000 box model simulations. (*A*) Model–data comparison scores (*S*; Eq. **6**), with gray contours of macronutrient usage efficiency (note the uneven contour interval). (*B*) Envelope of model–data comparison scores and (*C*) envelope of macronutrient use efficiency, both calculated from the median of simulations with equal $\gamma/\lambda \pm$ the median absolute deviation. The range of γ/λ informed by oceanic observations is indicated by arrows on the *x* axis. Best-fit simulations have an optimal γ/λ (4,398 s) marked by the vertical black dashed line. The optimum ratio lies within the data-constrained range of γ/λ, and within the iron and macronutient colimited regime identified in Fig. 4. The horizontal dashed line in *B* is a benchmark model–data comparison score (0.69) calculated from an instance where ligand concentration is a fixed, uniform, 1 μmol·m^{-3}. The horizontal dashed line in *C* is at the emergent value of macronutrient usage efficiency (0.29) at the optimal γ/λ ratio.

ligand pool. The ratio of aggregate ligand production and loss rates (γ/λ) is the critical parameter that controls the biogeochemical state of the global ocean. Our model suggests three major regimes: the "modern" regime with intermediate ligand lifetime and global-scale colimitation, a long-lived ligand regime with an iron-replete global ocean, and an iron-limited short-lived ligand regime where scarce chelators cannot maintain a standing stock of iron. Guiding γ/λ with observations, the hypothesized feedback drives the system into global-scale colimitation between iron and macronutrients (Fig. 3) reminiscent of the observed ocean (60), with relatively uniform ligand levels and slightly higher abundance in the upwelling regime (31, 64). Macronutrient use efficiency (0.29, range 0.22 to 0.40) is also consistent with the modern ocean value of 0.36 (9). Globally, the feedback maintains a pool of ligands that can support "just enough" iron to match the abundance of other resources, such as macronutrients, leading to global colimitation and maximized rates of production (Fig. 4).

We note that this highly idealized model represents the aggregate properties of what is a rich spectrum of chelating molecules with differing origins and cycles. Here we consider broad shifts in the overall properties of this suite of molecules, which is a practical choice that ought to be revisited as understanding of ligands and their cycles is revealed in the future. There are other properties of ligands, such as their conditional stability coefficient(s), which also vary but are not explicitly explored here. More-comprehensive approaches to modeling ligand cycles are being explored (e.g., ref. 64) and depend on determining constrained parameter values, for which the global GEOTRACES dataset (60) and target process studies identifying ligand sources and sinks and iron retention mechanisms (e.g., refs. 37, 38, and 68) should provide fundamental constraints.

There are analogies between the feedback suggested here, linking ligand and iron availability to macronutrient concentration at certain scales, and discussions of interplay between the nitrogen and phosphorus cycles (4–6). Our discussion parallels the perspective that phosphorus may be the ultimate limiting nutrient in the ocean, with nitrogen held close to Redfieldian proportions on the global scale through the balance of nitrogen fixation and denitrification (4–6). Our focus on iron means we assumed a fixed global macronutrient inventory and have not resolved this complex and subtle interplay. In practice, some interesting connections are likely, for example, through iron limitation of nitrogen fixation (5), and interactions with the oxygen cycle and redox chemistry. These could be addressed within a more complex modeling framework (69–71).

Keeping in mind simplifications of the model, a key inference is that the modern ocean falls into the intermediate nutrient regime, where ligand characteristics lead to global-scale macronutrient and iron colimitation. What sets the properties of the ligand pool? Could they reflect an evolutionary self-organization of the global ocean ecosystem?

Proterozoic oceans were likely rich in dissolved ferrous iron (Fe(II)) due to anoxia (72–74), but production was limited

Table 1. Fixed box model parameter values

Name	Symbol	Units	Value
No. of boxes	n_b		3
Latitudinal extent	y	m	3.0×10^6, 13.0×10^6, 16.0×10^6
Box thickness	z	m	50.0, 50.0, 5050.0
Box volume	v	m^3	3.4×10^{15}, 1.0×10^{16}, 1.4×10^{18}
Overturning rate	ψ	$m^3\cdot s^{-1}$	20.0×10^6
Mixing rate	κ	$m^3\cdot s^{-1}$	1.0×10^6
Maximum productivity	α	mol m^{-3} y^{-1}	5.1×10^{-4}
N half-saturation	k_N	mmol m^{-3}	0.1
Fe half-saturation	k_{Fe}	μmol m^{-3}	0.1
Light half-saturation	k_I	W m^{-2}	45.0
Fe source rate	s_{Fe}	mol $m^{-3}\cdot s^{-1}$	2.1×10^{-15}, 2.1×10^{-13}, 2.3×10^{-17}
Fe′ scavenging rate	k_s	s^{-1}	1.0×10^{-7}
L_T stability coefficient	β	m^3mol^{-1}	1.0×10^6
N reference mean	$\overline{N_0}$	mmol m^{-3}	24.0, 3.0, 31.6
Fe reference mean	$\overline{Fe_0}$	μmol m^{-3}	0.2, 0.3, 0.7
L_T reference mean	$\overline{L_{T0}}$	μmol m^{-3}	1.9, 2.0, 2.4
N reference SD	σ_{N_0}	mmol m^{-3}	3.7, 5.1, 11.5
Fe reference SD	σ_{Fe_0}	μmol m^{-3}	0.4, 0.3, 2.3
L_T reference SD	$\sigma_{L_{T0}}$	μmol m^{-3}	1.0, 0.9, 3.4

Triplets indicate values in the "Southern Ocean," "Atlantic Ocean," and "Deep Ocean" boxes, respectively.

by low concentrations of phosphate and nitrogen (75–79). It has been argued that nutrients were limiting due to several intertwined factors including slow remineralization in the absence of oxygen (80, 81), phosphate scavenging by abundant Fe(II) ions (78, 82), and suppression of nitrogen supply due to scavenging of molybdenum (83, 84), an essential nitrogen cycle cofactor, by sulfide ions in coastal environments (85, 86).

Around the Neoproterozoic (87, 88), ancient marine cyanobacteria expanded into the nutrient-poor oceans as evolutionary selection drove internal stoichiometry toward lower subsistence nutrient ratios and also increased exudation of dissolved organic carbon such as polysaccharides and carboxylic acids (89). The iron-chelating properties of organic carbon exudates may have initially promoted the release of phosphorus from dust by dissolution of iron minerals, which is a strategy some microbes employ today under phosphorus stress (90). As the ocean became oxygenated, these organic molecules may have facilitated the aerobic availability of Fe(III) by acting as iron-stabilizing ligands (43), helping photosynthesizers overcome a key negative feedback between oxygen-producing photoautotrophy and their dependency on iron (79). Enhancing supply of iron and organic carbon in nitrogen-poor surface oceans may have created new opportunities for nitrogen fixers (87), increasing oceanic nitrogen supply (75–77, 79).

Transitioning from an anoxic ocean rich in free Fe(II) to an oxygenated ocean with organic carbon-bound Fe(III) (79) would have initiated the "ligand–iron–microbe" feedback, with implications for nutrient consumption and ocean productivity.

Phanerozoic innovations continued to alter ocean ecosystem and marine iron chemistry interactions. Siderophore production and uptake genes are widely distributed in heterotrophic bacteria (91), while microbes that cannot produce competitively binding ligands, like some eukaryotic phytoplankton, developed methods to steal siderophore-bound iron by employing ligand nonspecific iron reductases (e.g., refs. 40, 44, 47, and 92). This suggests temporal variations in γ/λ.

The "ligand–iron–microbe" feedback may merit reassessment of the climatic effects of changing iron sources on atmospheric CO_2. We would anticipate little change to the global outcome of iron fertilization experiments when resolving dynamic ligands, because the ocean should already be at or near global colimitation with near-maximum export production, although local changes may occur to allow small atmospheric CO_2 anomalies (e.g., refs. 16–21). On longer timescales, the "ligand–iron–microbe" feedback could potentially act by self-amplifying or self-damping climatic changes, depending on the associated nutrient dynamics in the oceans. During ice ages (93), there may have been an increase in iron supply as well as greater macronutrient availability through possible erosion of exposed shelf sediments or greater marine nitrogen fixation (e.g., refs. 5, 8, 94, and 95). We predict that, under these conditions, the "ligand–iron–microbe" feedback would act in a self-amplifying manner, by increasing production of ligands and iron abundance so as to drive the system toward colimitation with macronutrients, maximizing productivity. In a warmer, more humid, and therefore less dusty climate (e.g., ref. 20), we, in turn, predict the "ligand–iron–microbe" feedback would first act to buffer the ocean from the effects of decreased iron supply by maintaining a high rate of production and thus ligand supply that extends the lifetime of iron. Once the global ocean transitions from the colimited regime into the iron-limited regime, the feedback might then exacerbate iron scarcity through reduction in productivity and declining ligand production.

Finally, we note that our proposed feedback could apply to other trace metals that are subject to chelation by organic ligands in the ocean. There is close correspondence between the stoichiometry of organic matter and available dissolved concentrations of trace metals (figure 1 in ref. 12), suggesting that the system may have coevolved to optimize micronutrient supply and demand for several other trace elements (26, 96, 97). Perhaps there is also "just enough" of these other micronutrients in the ocean to match levels of the more abundant macronutrients, promote global resource colimitation, and maximize production.

Materials and Methods

An idealized model (Fig. 2) is used to efficiently explore the "ligand–iron–microbe" feedback. There are two asymmetrical surface boxes as well as a global deep ocean box linked by an overturning circulation (ψ). Deep water formation occurs in the "Atlantic Ocean" with upwelling in the "Southern Ocean". These boxes are named for ease of reference, but the overall concepts could equally apply to other regions. A flux due to mixing (κ) also occurs. See Table 1 for parameter values.

Net production (B) is modeled using Michaelis–Menten kinetics (Eq. **1**), with maximum rate, α, and potentially limited by macronutrients (Eq. **2**), iron (Eq. **3**), or light, with half-saturation coefficients, k_N, k_{Fe}, and k_I.

Iron is asymetrically supplied to the surface (s_{Fe}), representing aeolian dust (50) or sediment (51) sources. A hydrothermal iron source [1 Gmol $Fe \cdot y^{-1}$ (53)] is also added to the deep ocean.

For illustrative purposes, we consider a single dynamic, representative pool of ligand (Eq. **4**) with a conditional stability coefficient (β) that determines partitioning between free (Fe' and L') and complexed (FeL) iron and ligands (49): $\beta = [FeL]/[Fe'][L']$. Free iron is scavenged and precipitated when in excess of its low solubility with rate constant k_s. Ligand cycling is described by Eq. **4**.

Our model suite comprises 10,000 simulations of 10,000 y, each with different rates of ligand production (γ) between 1×10^{-7} and 1×10^{-1} and ligand loss ($1/\lambda$) between 0.1 y and 1,000 y. The rate of ligand loss is modified to be 100 times smaller in the deep box than in the surface box (55) to account for the gradient resulting from enhanced depletion by photochemical degradation (24, 56) and microbial ligand uptake (57) in the upper ocean, slower losses due to an order of magnitude decrease in bacterial abundance (58), and slower metabolism resulting from cooler temperatures, at depth. The global macronutrient inventory is conserved, with initial concentrations randomly assigned a fraction of the total inventory. Iron and ligand levels were randomly assigned between 0 $\mu mol \cdot m^{-3}$ and 100 $\mu mol \cdot m^{-3}$.

Simulations are scored by their resemblance to oceanic observations (Eq. **6**) for equally weighted, steady-state macronutrient, iron, and ligand concentrations. Reference values (N_0, Fe_{T0}, and L_{T0}) are averages and standard deviations from representative geographic areas for each box using World Ocean Atlas 2013 (98) for nitrate and using the GEOTRACES intermediate data product 2017 (60) for iron and ligands. Owing to paucity of ligand data in the Southern Ocean, $\overline{L_{T0}}$ and $\sigma_{L_{T0}}$ comprise data from the entire Southern Hemisphere.

$$ln(S) = -\frac{1}{3n_b}\left(\sum_{n_b}\frac{\Delta N^2}{\sigma_{N_0}^2} + \sum_{n_b}\frac{\Delta Fe_T{}^2}{\sigma_{Fe_{T0}}^2} + \sum_{n_b}\frac{\Delta L_T{}^2}{\sigma_{L_{T0}}^2}\right), \qquad [6]$$

where $\Delta N = [N] - \overline{N_0}$, $\Delta Fe_T = [Fe_T] - \overline{Fe_{T0}}$, and $\Delta L_T = [L_T] - \overline{L_{T0}}$.

Our overall characterization of the "ligand–iron–microbe" feedback is insensitive to geometry, circulation, or biogeochemistry parameters, although the exact details vary for choices of β and s_{Fe}.

Model code, output, and processing routines can be accessed via GitHub (http://bit.ly/lauderdale-ligand-iron-microbe-feedback) (99).

ACKNOWLEDGMENTS. We are grateful to GEOTRACES program scientists, technicians, and crew for oceanic trace metal and ligand observations. We acknowledge funding from the NSF Partnerships for International Research and Education Program (Grant 1545859, J.M.L.), Gordon and Betty Moore Foundation (Award 3778, M.J.F.), Simons Foundation (Life Sciences Project Award to S. W. Chisholm, Grant 509034SCFY17, R.B.), Simons Collaboration on Ocean Processes and Ecology (Award 329108, M.J.F.), and Simons Collaboration on Computational Biogeochemical Modeling of Marine Ecosystems (Award 549931, M.J.F.). We are very grateful for encouragement and discussion from Ric Williams. We thank two anonymous reviewers for their feedback, as well as Ed Boyle, Curtis Deutsch, Taka Ito, and Ahn Pham for discussions that also improved this manuscript.

1. J. H. Martin, S. E. Fitzwater, Iron deficiency limits phytoplankton growth in the north-east Pacific subarctic. *Nature* **331**, 341–343 (1988).
2. K. H. Coale *et al.*, A massive phytoplankton bloom induced by an ecosystem-scale iron fertilization experiment in the equatorial Pacific Ocean. *Nature* **383**, 495–501 (1996).
3. P. W. Boyd *et al.*, A mesoscale phytoplankton bloom in the polar Southern Ocean stimulated by iron fertilization. *Nature* **407**, 695–702 (2000).
4. T. Tyrrell, The relative influences of nitrogen and phosphorus on oceanic primary production. *Nature* **400**, 525–531 (1999).
5. P. G. Falkowski, Evolution of the Nitrogen Cycle and its influence on the biological sequestration of CO_2 in the ocean. *Nature* **387**, 272–275 (1997).
6. N. Gruber, "The marine nitrogen cycle: Overview and challenges" in *Nitrogen in the Marine Environment*, D. G. Capone, D. A. Bronk, M. R. Mulholland, E. J. Carpenter, Eds. (Academic, San Diego, CA, 2008), pp. 1–50.
7. A. C. Redfield, B. H. Ketchum, F. A. Richards, "The influence of organisms on the composition of sea-water" in *The Sea: The Composition of Seawater. Comparative and Descriptive Oceanography*, M. N. Hill, Ed. (Wiley-Interscience: New York, NY, 1963), vol. 2, pp. 26–77.
8. D. M. Sigman, E. A. Boyle, Glacial/interglacial variations in atmospheric carbon dioxide. *Nature* **407**, 859–869 (2000).
9. T. Ito, M. J. Follows, Preformed phosphate, soft tissue pump and atmospheric CO_2. *J. Mar. Res.* **63**, 813–839 (2005).
10. J. K. Moore, S. C. Doney, D. M. Glover, I. Y. Fung, Iron cycling and nutrient-limitation patterns in surface waters of the world ocean. *Deep Sea Res. Part II* **49**, 463–507 (2002).
11. O. Aumont, E. Maier-Reimer, S. Blain, P. Monfray, An ecosystem model of the global ocean including Fe, Si, P colimitations. *Global Biogeochem. Cycles* **17**, 1060 (2003).
12. C. M. Moore *et al.*, Processes and patterns of oceanic nutrient limitation. *Nat. Geosci.* **6**, 701–710 (2013).
13. X. Liu, F. J. Millero, The solubility of iron in seawater. *Mar. Chem.* **77**, 43–54 (2002).
14. K. W. Bruland, K. J. Orians, J. P. Cowen, Reactive trace metals in the stratified central North Pacific. *Geochem. Cosmochim. Acta* **58**, 3171–3182 (1994).
15. K. S. Johnson, R. M. Gordon, K. H. Coale, What controls dissolved iron concentrations in the world ocean?*Mar. Chem.* **57**, 137–161 (1997).
16. N. Lefèvre, A. J. Watson, Modeling the geochemical cycle of iron in the oceans and its impact on atmospheric CO_2 concentrations. *Global Biogeochem. Cycles* **13**, 727–736 (1999).
17. A. J. Watson, D. C. E. Bakker, A. J. Ridgwell, P. W. Boyd, C. S. Law, Effect of iron supply on Southern Ocean CO_2 uptake and implications for glacial atmospheric CO_2. *Nature* **407**, 730–733 (2000).
18. L. Bopp, K. E. Kohfeld, C. Le Quéré, O. Aumont, Dust impact on marine biota and atmospheric CO_2 during glacial periods. *Paleoceanography* **18**, 1046 (2003).
19. R. E. Zeebe, D. Archer, Feasibility of ocean fertilization and its impact on future atmospheric CO_2 levels. *Geophys. Res. Lett.* **32**, L09703 (2005).
20. P. Parekh, M. J. Follows, S. Dutkiewicz, T. Ito, Physical and biological regulation of the soft tissue carbon pump. *Paleoceanography* **21**, PA3001 (2006).
21. O. Aumont, L. Bopp, Globalizing results from ocean in situ iron fertilization studies. *Global Biogeochem. Cycles* **20**, GB2017 (2006).
22. S. Dutkiewicz, M. J. Follows, P. Parekh, Interactions of the iron and phosphorus cycles: A three dimensional model study. *Global Biogeochem. Cycles* **19**, GB1021 (2005).
23. E. L. Rue, K. W. Bruland, Complexation of iron(III) by natural organic ligands in the Central North Pacific as determined by a new competitive ligand equilibration/adsorptive cathodic stripping voltammetric method. *Mar. Chem.* **50**, 117–138 (1995).
24. E. L. Rue, K. W. Bruland, The role of organic complexation on ambient iron chemistry in the equatorial Pacific Ocean and the response of a mesoscale iron addition experiment. *Limnol. Oceanogr.* **42**, 901–910 (1997).
25. K. A. Hunter, P. W. Boyd, Iron-binding ligands and their role in the ocean biogeochemistry of iron. *Environ. Chem.* **4**, 221–232 (2007).
26. J. M. Vraspir, A. Butler, Chemistry of marine ligands and siderophores. *Annu. Rev. Mar. Sci.* **1**, 43–63 (2009).
27. C. S. Hassler, V. Schoemann, C. M. Nichols, E. C. V. Butler, P. W. Boyd, Saccharides enhance iron bioavailability to Southern Ocean phytoplankton. *Proc. Natl. Acad. Sci. U.S.A.* **108**, 1076 (2011).
28. M. Gledhill, K. N. Buck, The organic complexation of iron in the marine environment: A review. *Front. Microbiol.* **3**, 69 (2012).
29. K. N. Buck, B. Sohst, P. N. Sedwick, The organic complexation of dissolved iron along the U.S. GEOTRACES (GA03) North Atlantic Section. *Deep Sea Res. Part II* **116**, 152–165 (2015).
30. L. J. A. Gerringa, M. J. A. Rijkenberg, V. Schoemann, P. Laan, H. J. W. de Baar, Organic complexation of iron in the West Atlantic Ocean. *Mar. Chem.* **177**, 434–446 (2015).
31. K. N. Buck, P. N. Sedwick, B. Sohst, C. A. Carlson, Organic complexation of iron in the eastern tropical south pacific: Results from US GEOTRACES Eastern Pacific Zonal Transect (GEOTRACES cruise GP16). *Mar. Chem.* **201**, 229–241 (2018).
32. C. S. Hassler, C. M. G. van den Berg, P. W. Boyd, Toward a regional classification to provide a more inclusive examination of the ocean biogeochemistry of iron-binding ligands. *Front. Mar. Sci.* **4**, 19 (2017).
33. R. M. Boiteau, J. N. Fitzsimmons, D. J. Repeta, E. A. Boyle, Detection of iron ligands in seawater and marine cyanobacteria cultures by high-performance liquid chromatography–inductively coupled plasma-mass spectrometry. *Anal. Chem.* **85**, 4357–4362 (2013).
34. R. M. Boiteau, D. J. Repeta, An extended siderophore suite from Synechococcus sp. PCC 7002 revealed by LC–ICPMS–ESIMS. *Metallomics* **7**, 877–884 (2015).
35. R. M. Bundy *et al.*, Iron-binding ligands and humic substances in the San Francisco Bay estuary and estuarine-influenced shelf regions of coastal California. *Mar. Chem.* **173**, 183–194 (2015).
36. I. Pižeta *et al.*, Interpretation of complexometric titration data: An intercomparison of methods for estimating models of trace metal complexation by natural organic ligands. *Mar. Chem.* **173**, 3–24 (2015).
37. R. M. Bundy *et al.*, Distinct siderophores contribute to iron cycling in the mesopelagic at station ALOHA. *Front. Mar. Sci.* **5**, 61 (2018).
38. R. M. Boiteau *et al.*, Patterns of iron and siderophore distributions across the California current system. *Limnol. Oceanogr.* **64**, 376–389 (2019).
39. M. Gledhill *et al.*, Production of siderophore type chelates by mixed bacterioplankton populations in nutrient enriched seawater incubations. *Mar. Chem.* **88**, 75–83 (2004).
40. J. S. Martinez, M. G. Haygood, A. Butler, Identification of a natural desferrioxamine siderophore produced by a marine bacterium. *Limnol. Oceanogr.* **46**, 420–424 (2001).
41. R. M. Boiteau *et al.*, Siderophore-based microbial adaptations to iron scarcity across the eastern Pacific Ocean. *Proc. Natl. Acad. Sci. U.S.A.* **113**, 14237–14242 (2016).
42. D. A. Hutchins, A. E. Witter, A. Butler, G. W. Luther III, Competition among marine phytoplankton for different chelated iron species. *Nature* **400**, 858–861 (1999).
43. M. Chen, W.-X. Wang, L. Guo, Phase partitioning and solubility of iron in natural seawater controlled by dissolved organic matter. *Global Biogeochem. Cycles* **18**, GB4013 (2004).
44. B. M. Hopkinson, F. M. M. Morel, The role of siderophores in iron acquisition by photosynthetic marine microorganisms. *Biometals* **22**, 659–669 (2009).
45. L. M. Laglera, C. M. G. van den Berg, Evidence for geochemical control of iron by humic substances in seawater. *Limnol. Oceanogr.* **54**, 610–619 (2009).
46. P. W. Boyd, E. Ibisanmi, S. G. Sander, K. A. Hunter, G. A. Jackson, Remineralization of upper ocean particles: Implications for iron biogeochemistry. *Limnol. Oceanogr.* **55**, 1271–1288 (2010).
47. M. Boye *et al.*, Major deviations of iron complexation during 22 days of a mesoscale iron enrichment in the open Southern Ocean. *Mar. Chem.* **96**, 257–271 (2005).
48. Y. Kondo *et al.*, Organic iron(III) complexing ligands during an iron enrichment experiment in the western subarctic North Pacific. *Geophys. Res. Lett.* **35**, L12601 (2008).
49. P. Parekh, M. J. Follows, E. A. Boyle, Decoupling of iron and phosphate in the global ocean. *Global Biogeochem. Cycles* **19**, GB2020 (2005).
50. N. M. Mahowald *et al.*, Change in atmospheric mineral aerosols in response to climate: Last glacial period, preindustrial, modern and doubled carbon dioxide climates. *J. Geophys. Res.* **111**, D10202 (2006).
51. V. A. Elrod, W. M. Berelson, K. H. Coale, K. S. Johnson, The flux of iron from continental shelf sediments: A missing source for global budgets. *Geophys. Res. Lett.* **31**, L12307 (2004).
52. P. Parekh, M. J. Follows, E. Boyle, Modeling the global ocean iron cycle. *Global Biogeochem. Cycles* **18**, GB1002 (2004).
53. A. Tagliabue *et al.*, Hydrothermal contribution to the oceanic dissolved iron inventory. *Nat. Geosci.* **3**, 252–256 (2010).
54. S. A. Amin *et al.*, Photolysis of iron–siderophore chelates promotes bacterial–algal mutualism. *Proc. Natl. Acad. Sci. U.S.A.* **106**, 17071–17076 (2009).
55. Y. Ye, C. Völker, D. A. Wolf-Gladrow, A model of Fe speciation and biogeochemistry at the tropical eastern North Atlantic time-series observatory site. *Biogeosciences* **6**, 2041–2061 (2009).
56. M. Boye *et al.*, Organic complexation of iron in the Southern Ocean. *Deep Sea Res. Part I* **48**, 1477–1497 (2001).
57. M. T. Maldonado, N. M. Price, Utilization of iron bound to strong organic ligands by plankton communities in the subarctic Pacific Ocean. *Deep Sea Res. Part II* **46**, 2447–2473 (1999).
58. A. Yamaguchi *et al.*, Structure and size distribution of plankton communities down to the greater depths in the western North Pacific Ocean. *Deep Sea Res. Part II* **49**, 5513–5529 (2002).
59. C. B. Field, M. J. Behrenfeld, J. T. Randerson, P. Falkowski, Primary production of the biosphere: Integrating terrestrial and oceanic components. *Science* **281**, 237–240 (1998).
60. R. Schlitzer *et al.*, The GEOTRACES intermediate data product 2017. *Chem. Geol.* **493**, 210–223 (2018).
61. B. W. Eakins, G. F. Sharman, Volumes of the world's oceans from ETOPO1. *NOAA National Geophysical Data Center* (2010). https://www.ngdc.noaa.gov/mgg/global/etopo1_ocean_volumes.html. Accessed 16 January 2018.
62. T. Wagener, E. Pulido-Villena, C. Guieu, Dust iron dissolution in seawater: Results from a one-year time-series in the Mediterranean Sea. *Geophys. Res. Lett.* **35**, L16601 (2008).
63. C. Schlosser, P. L. Croot, Controls on seawater Fe(III) solubility in the Mauritanian upwelling zone. *Geophys. Res. Lett.* **36**, L18606 (2009).
64. C. Völker, A. Tagliabue, Modeling organic iron-binding ligands in a three-dimensional biogeochemical ocean model. *Mar. Chem.* **173**, 67–77 (2015).
65. A. Tagliabue *et al.*, How well do global ocean biogeochemistry models simulate dissolved iron distributions?*Global Biogeochem. Cycles* **30**, 149–174 (2016).
66. J. L. Sarmiento, J. R. Toggweiler, A new model for the role of the oceans in determining atmospheric pCO_2. *Nature* **308**, 621–624 (1984).
67. F. Knox, M. B. McElroy, Changes in atmospheric CO_2: Influence of the marine biota at high latitude. *J. Geophys. Res.* **89**, 4629–4637 (1984).
68. M. P. Fishwick *et al.*, The impact of changing surface ocean conditions on the dissolution of aerosol iron. *Global Biogeochem. Cycles* **28**, 1235–1250 (2014).
69. M. J. Follows, S. Dutkiewicz, S. Grant, S. W. Chisholm, Emergent biogeography of microbial communities in a model ocean. *Science* **315**, 1843–1846 (2007).

70. F. M. Monteiro, M. J. Follows, S. Dutkiewicz, Distribution of diverse nitrogen fixers in the global ocean. *Global Biogeochem. Cycles* **24**, GB3017 (2010).
71. B. A. Ward, S. Dutkiewicz, O. Jahn, M. J. Follows, A size-structured food-web model for the global ocean. *Limnol. Oceanogr.* **57**, 1877–1891 (2012).
72. D. E. Canfield *et al.*, Ferruginous conditions dominated later neoproterozoic deep-water chemistry. *Science* **321**, 949–952 (2008).
73. N. J. Planavsky *et al.*, Widespread iron-rich conditions in the mid-Proterozoic ocean. *Nature* **477**, 448–451 (2011).
74. E. A. Sperling *et al.*, Statistical analysis of iron geochemical data suggests limited late proterozoic oxygenation. *Nature* **523**, 451–454 (2015).
75. E. E. Stüeken, A test of the nitrogen-limitation hypothesis for retarded eukaryote radiation: Nitrogen isotopes across a mesoproterozoic basinal profile. *Geochem. Cosmochim. Acta* **120**, 121–139 (2013).
76. M. Ader *et al.*, Ocean redox structure across the Late Neoproterozoic oxygenation event: A nitrogen isotope perspective. *Earth Planet Sci. Lett.* **396**, 1–13 (2014).
77. M. C. Koehler, E. E. Stüeken, M. A. Kipp, R. Buick, A. H. Knoll, Spatial and temporal trends in Precambrian nitrogen cycling: A Mesoproterozoic offshore nitrate minimum. *Geochem. Cosmochim. Acta* **198**, 315–337 (2017).
78. C. T. Reinhard *et al.*, Evolution of the global phosphorus cycle. *Nature* **541**, 386–389 (2016).
79. R. Braakman, Evolution of cellular metabolism and the rise of a globally productive biosphere. *Free Radical Biol. Med.* **140**, 172–187 (2019).
80. K. Fennel, M. Follows, P. G. Falkowski, The co-evolution of the nitrogen, carbon and oxygen cycles in the Proterozoic ocean. *Am. J. Sci.* **305**, 526–545 (2005).
81. M. A. Kipp, E. E. Stüeken, Biomass recycling and Earth's early phosphorus cycle. *Sci. Adv.* **3**, eaao4795 (2017).
82. C. J. Bjerrum, D. E. Canfield, Ocean productivity before about 1.9 Gyr ago limited by phosphorus adsorption onto iron oxides. *Nature* **417**, 159–162 (2002).
83. C. Scott *et al.*, Tracing the stepwise oxygenation of the Proterozoic ocean. *Nature* **452**, 456–459 (2008).
84. R. R. Large *et al.*, Trace element content of sedimentary pyrite as a new proxy for deep-time ocean–atmosphere evolution. *Earth Planet Sci. Lett.* **389**, 209–220 (2014).
85. A. D. Anbar, A. H. Knoll, Proterozoic ocean chemistry and evolution: A bioinorganic bridge? *Science* **297**, 1137–1142 (2002).
86. C. T. Reinhard *et al.*, Proterozoic ocean redox and biogeochemical stasis. *Proc. Natl. Acad. Sci. U.S.A.* **110**, 5357–5362 (2013).
87. P. Sánchez-Baracaldo, A. Ridgwell, J. A. Raven, A Neoproterozoic transition in the marine nitrogen cycle. *Curr. Biol.* **24**, 652–657 (2014).
88. P. Sánchez-Baracaldo, Origin of marine planktonic cyanobacteria. *Sci. Rep.* **5**, 17418 (2015).
89. R. Braakman, M. J. Follows, S. W. Chisholm, Metabolic evolution and the self-organization of ecosystems. *Proc. Natl. Acad. Sci. U.S.A.* **114**, E3091 (2017).
90. S. Romano, V. Bondarev, M. Kölling, T. Dittmar, H. N. Schulz-Vogt, Phosphate limitation triggers the dissolution of precipitated iron by the marine bacterium pseudovibrio sp. FO-BEG1. *Front. Microbiol.* **8**, 364–375 (2017).
91. R. C. Hider, X. Kong, Chemistry and biology of siderophores. *Nat. Prod. Rep.* **27**, 637–657 (2010).
92. T. H. Coale *et al.*, Reduction-dependent siderophore assimilation in a model pennate diatom. *Proc. Natl. Acad. Sci. U.S.A.* **116**, 23609–23617 (2019).
93. J. H. Martin, Glacial–interglacial CO_2 change: The iron hypothesis. *Paleoceanography* **5**, 1–13 (1990).
94. W. S. Broecker, Glacial to interglacial changes in ocean chemistry. *Prog. Oceanogr.* **11**, 151–197 (1982).
95. S. Peacock, E. Lane, J. M. Restrepo, A possible sequence of events for the generalized glacial-interglacial cycle. *Global Biogeochem. Cycles* **20**, GB2010 (2006).
96. F. M. M. Morel, N. M. Price, The biogeochemical cycles of trace metals. *Science* **300**, 944–947 (2003).
97. N. J. Planavsky, The elements of marine life. *Nat. Geosci.* **7**, 855–856 (2014).
98. H. E. Garcia *et al.*, *Dissolved Inorganic Nutrients (Phosphate, Nitrate, Silicate)* (World Ocean Atlas 2013, National Oceanic and Atmospheric Administration, 2014), vol. 4.
99. J. M. Lauderdale, R. Braakman, G. Forget, S. Dutkiewicz, M. J. Follows, Box model code, analysis routines, and large model ensemble data characterizing the "ligand-iron-microbe" feedback. GitHub. http://bit.ly/lauderdale-ligand-iron-microbe-feedback. Deposited 11 September 2019.